ORNL/SPR-2024-3523
M3LW-24OR0402053

Light Water Reactor Sustainability Program

In-service Oxidation and IASCC in High Fluence Baffle-Former Bolts Retrieved from a Westinghouse PWR

Timothy G. Lach
Maxim N. Gussev
Xiang (Frank) Chen

August 2024

U.S. Department of Energy
Office of Nuclear Energy

ORNL/SPR-2024-3523
M3LW-24OR0402053

Light Water Reactor Sustainability (LWRS) Program
Materials Research Pathway

IN-SERVICE OXIDATION AND IASCC IN HIGH FLUENCE BAFFLE-FORMER BOLTS RETRIEVED FROM A WESTINGHOUSE PWR

Timothy G. Lach[1], Maxim N. Gussev[2], Xiang (Frank) Chen[1]

[1]Materials Science and Technology Division
[2]Nuclear Energy and Fuel Cycle Division
Oak Ridge National Laboratory

August 2024

Prepared by
OAK RIDGE NATIONAL LABORATORY
Oak Ridge, TN 37831-6136
managed by
UT-BATTELLE LLC
for the
US DEPARTMENT OF ENERGY
under contract DE-AC05-00OR22725

CONTENTS

LIST OF FIGURES

LIST OF TABLES

ACKNOWLEDGMENT

This research was sponsored by the U.S. Department of Energy, Office of Nuclear Energy, Light Water Reactor Sustainability Program, Materials Research Pathway, under contract DE-AC05-00OR22725 with UT-Battelle, LLC/Oak Ridge National Laboratory (ORNL).

The authors extend their appreciation to Clay Morris, Jerid Metcalf, and other colleagues at Irradiated Materials Examination and Testing Facility (IMET) at ORNL for their support of sample processing during the hot cell sample retrieval. In addition, we would like to thank Patricia Tedder, Kyle Everett, and Travis Dixon at the Low Activation Materials Development and Analysis (LAMDA) laboratory at ORNL for receiving, cleaning, inventorying, and polishing the irradiated samples. Lastly, we would like to thank the late Mike Burke formerly with Electrical Power Research Institute who was involved in the bolt harvesting and characterization planning and led the sample preparation, machining, and shipping when he was working at Westinghouse Electric Company.

EXECUTIVE SUMMARY

Baffle-former bolts (BFBs) are subjected to significant mechanical stress and neutron irradiation from the reactor core during the plant operation. Over the long operation period, these conditions lead to potential degradation and reduced load-carrying capacity of the bolts, and life extension of existing pressurized water reactors (PWRs) would only cause more damage to the bolt material. To this end, the Light Water Reactor Sustainability (LWRS) Program Materials Research Pathway (MRP) successfully harvested two high fluence BFBs from a Westinghouse two-loop downflow type PWR in 2016. In the same year, the two BFBs were received at the Westinghouse Churchill facility for inspection and specimen fabrication. The fabrication was completed in 2017 with specimens shipped to Oak Ridge National Laboratory (ORNL) for further testing. The objective of this project is to provide information that is integral to evaluating end of life microstructure and properties as a benchmark of international models developed for predicting radiation-induced swelling, segregation, precipitation, mechanical property degradation, and with the latest findings, susceptibility to irradiation-assisted stress corrosion cracking (IASCC).

In this report, we present our latest study in FY24 on microstructural characterizations of surface oxidation and IASCC at the intersection of the bolt head and the bolt shank in both high fluence BFBs.: general oxidation, grain boundary attack, and localized deformation via dislocation channeling. The main findings are summarized as follows:

1. Complex multilayered surface oxide formation: The surface oxide is ~2-3 μm thick depending on the bolt with five – not three – distinct layers that vary based on composition and grain size. The innermost layer is Cr-rich and Fe/Ni depleted. The next layer is both Cr and Fe/Ni-rich and is too monolithic in nature. In previous studies, these two layers are likely seen as one layer but are clearly found to be distinct here. The next two layers are also likely commonly seen as the same layer, but these Cr-rich and Fe/Ni-rich oxide layers are clearly distinguished primarily by grain size, with layer 3 being nanocrystalline and layer 4 being above ~100 nm in size. Layer 3 also was shown to vary most in its thickness between the two BFBs. Lastly, the outermost oxide is a Fe-rich oxide with large grain size of ~500 nm.
2. Grain boundary attack and pathway to outer oxide: The oxidized grain boundary attack features a pathway from the original grain boundary that is enriched in Fe/Ni and depleted in Cr that acts as a pathway for Fe/Ni to the outermost oxide layers. The grains along this path interrupt the nanocrystalline interior oxide layers as they are larger and depleted in Cr.
3. Localized deformation and elemental segregation: Localized deformation in the form of dislocation channels and deformation twins were observed. Along these channels, particularly the twinned channels, enhanced segregation and precipitation of Ni/Si was observed on the channel walls. The channels likely formed through heavy localized deformation clearing out defects. The channel eventually became less active, but radiation continued enabling diffusion, precipitation, and defect formation to resume in the vicinity of the channels. This could have implications for influencing segregation to grain boundaries and impacting susceptibility to IASCC.

1. INTRODUCTION

As one of the pressurized water reactor (PWR) internal components, baffle-former bolts (BFBs) are subjected to significant mechanical stress and neutron irradiation from the reactor core during the plant operation. Over the long operation period, these conditions lead to potential degradation and reduced load-carrying capacity of the bolts, and life extension of existing PWRs would only cause more damage to the bolt material. Indeed, the BFB has been a particular concern for the nuclear industry since the first observation of failed bolts following the investigation of flow-induced vibration of fuel rods in elements on the core periphery observed in French 900 MW plants in the 1980s [1]. In the United States, the first degraded BFBs were observed in 1999. In support of evaluating long-term operation performance of materials used in core internal components, the Materials Research Pathway (MRP) under the U.S. Department of Energy (DOE), Office of Nuclear Energy, Light Water Reactor Sustainability (LWRS) Program pursued the retrieval of aged structural components for the study of the microstructure, mechanical, and corrosion-related properties. To this end, the MRP successfully harvested two high fluence BFBs from a Westinghouse two-loop downflow type PWR in 2016. In the same year, the two BFBs were received at the Westinghouse Churchill facility for inspection and specimen fabrication. The fabrication was completed in 2017 with specimens shipped to Oak Ridge National Laboratory (ORNL) for further testing.

In this report, we present our latest study in FY24 on microstructural characterizations of surface oxidation and irradiation-assisted stress corrosion cracking (IASCC) at the intersection of the bolt head and the bolt shank in both high fluence BFBs. The objective of this project is to provide information that is integral to evaluating end of life microstructure and properties as a benchmark of international models developed for predicting radiation-induced swelling, segregation, precipitation, and mechanical property degradation. This project task performed characterizations in FY19 [2], FY22 [3], and FY23 [4] which focused on electron microscopy and atom probe tomography-based microstructural characterizations and microhardness testing for both harvested BFBs. Fracture toughness and fatigue crack growth rate testing results of both BFBs have also been published in the FY21 milestone report [5] for this project. This previous work from this task filled the knowledge gaps for radiation-induced microstructural evolution and mechanical property evolution. The results showed that radiation-induced precipitation, dislocation loop formation, and nanocavity evolution in the two BFBs was highly complex, with the volume fraction and size of Ni/Si and Cu-rich precipitates, dislocation loops, and nanocavities depending strongly on the radiation temperature/dose. The bolt thread end in each bolt had larger precipitates, loops, and nanocavities than the bolt head end. Specifically for clustering, comparing the two bolts, clustering was essentially the same for both bolts in the CS or bolt head section, but Ni/Si clustering was much higher in the BS or bolt thread section in the high dose bolt #4412 than in the lower dose bolt #4416.

Here, results from FY24 are presented on the study of in-service IASCC via scanning electron microscopy (SEM)-electron backscatter diffraction (EBSD) and energy dispersive X-ray spectroscopy (EDS) imaging and mapping, transmission electron microscopy (TEM), and analytical scanning TEM (STEM) at the intersection of the bolt head and bolt shank in the higher dose bolt which was exposed to primary coolant water. IASCC requires an environmentally-susceptible material, a corrosive environment, radiation, and mechanical stress. The bolt head/shank intersection in PWR BFBs meets all four requirements. This work highlights the features such as thick surface oxidation, grain boundary attack, and localized deformation that has been observed in laboratory-based research [6], but also aspects of these features that to the authors' knowledge has not been observed previously.

2. EXPERIMENTAL METHODS

2.1 Materials

The two harvested BFBs had the highest fluence among bolts withdrawn from service in 2011. Both bolts showed no indication of cracking during the ultrasonic inspection and in visual inspection following removal from service. However, the bolts required a lower torque for removal from the baffle structure than the original torque specified during installation. ***Figure 1*** shows images of the bolt heads of two retrieved BFBs; no indication of surface cracking was observed in the transition region between the shaft and head, although some surface debris scale flaked off from the bolt body. The shiny gray portion of the bolt head was due to electric discharge machining (EDM) when the bolts were removed from the baffle wall. However, both bolts do still have some of the original surface that was exposed to coolant water where the bolt head intersects with the bolt shank, as circled in ***Figure 1***b. The ID number for the bolts follows a 4-digit code with the first number being the quadrant location in the reactor, then the associated baffle plate number, the column location of the bolt associated with the particular baffle plate number, and finally the former plate location where the bolt originated. The composition in both atomic percent (at%) and weight percent (wt%) for both bolts as determined by APT is presented in Table 1 These bolts are within the specifications for type 316-SS with slightly elevated Cr content, but this could be due to local variations.

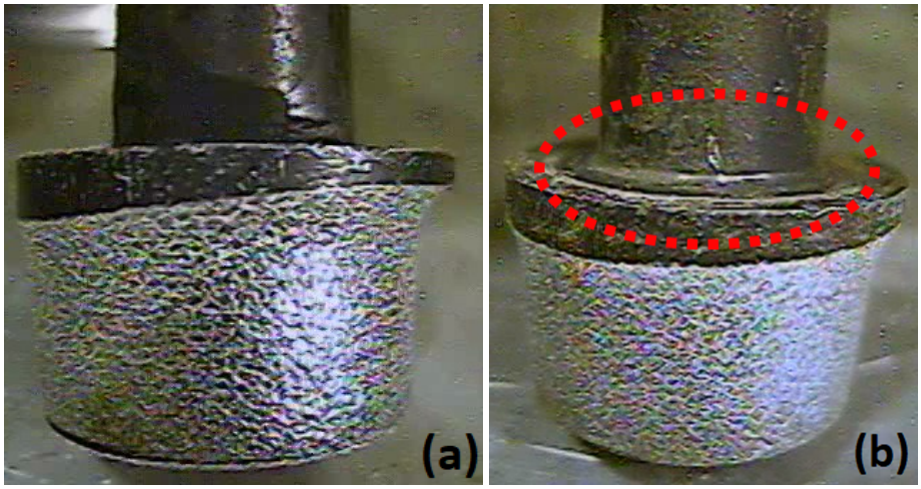

Figure 1*: Images of bolt heads for bolt #4412 in (a) and bolt #4416 in (b). Surface of bolt at bolt head/shank intersection (circled) was exposed to primary water and is still intact* [7]

Table 1*: Average compositions of bolt 4412 and 4416 from APT reconstructions for each bolt* [8] *in comparison with material specification (wt%) for 316 SS*

	BFB-4412		BFB-4416		316-SS Spec
Element	At%	Wt%	At%	Wt%	Wt%
Fe	64.19	64.62	64.56	64.96	Bal.
Ni	11.55	12.22	11.39	12.04	10.00-14.00
Cr	19.32	18.11	19.36	18.14	16.00-18.00
Mn	1.62	1.60	1.67	1.65	2.00 max
Mo	1.18	2.04	1.18	2.04	2.00-3.00
Si	1.24	0.63	1.15	0.58	1.00 max
C	0.20	0.043	0.19	0.040	0.08 max

P	0.024	0.013	0.027	0.015	0.040 max
Cu	0.26	0.29	0.25	0.28	0.75 max

Table 2 provides information on the range of fluences and estimated displacement damage along the length of the two bolts. The displacement damage values for the two bolts range from 15 to 41 displacements per atom (dpa) assuming a fluence to dpa conversion value of 6.7×10^{20} n/cm^2, E > 1 MeV per dpa [9]. Other important information for the two retrieved bolts not available at the time of preparation of this report includes the irradiation temperature profile, irradiation flux, and thermomechanical stress state. These require more complicated modeling and calculation and can vary within each power cycle and from cycle to cycle. For instance, calculations [10] from Point Beach Unit 2, which is another Westinghouse two-loop type PWR, showed that the irradiation temperature and flux for a BFB from a region next to the bolt 4416 studied in this work varied in the range of 323-344 °C and 7.5×10^{12}-1.8×10^{13} n/cm^2-sec (E > 1 MeV) along the length of the bolt, respectively. Similarly, a baffle-former bolt removed from the Tihange 1 PWR showed a variation in irradiation temperature of about 23 °C (320-343 °C) along the bolt and a damage dose that was 2.6X higher in the bolt head (19.5 dpa) than the bolt thread (7.5 dpa) [11]. Therefore, the value for a detailed calculation on irradiation temperature and flux of BFBs may be limited due to the large variation of those parameters during the lifetime of a BFB. It should be noted that Point Beach Unit 2 was originally a Westinghouse two-loop downflow type PWR but was converted to upflow in 1986 [10].

Table 2*: Fluence and estimated displacement damage distributions for two retrieved BFBs*

Bolt #	Fluence (10^{22} n/cm^2, E > 1 MeV)/Estimated dpa		
	Head	Mid-shank	Mid-thread
4412	2.78/41	2.27/34	1.46/22
4416	1.91/29	1.56/23	1.00/15

The specimen machining plan is shown in Figure 2. For each BFB, four bend bar specimens and seven thin slice specimens were machined. The bend bar specimens were used in the fracture toughness and fatigue crack growth rate studies, whereas the thin slice specimens are planned for subscale tensile and microstructural analyses. Specimens were machined from different fluence regions of each bolt, allowing for studies of the effect of fluence on the microstructural and mechanical properties of BFBs. Three thin slice specimens were machined from the high-stress concentration region, i.e., the transition between the bolt head and shank, of each bolt to allow for further investigation of possible crack initiation sites.

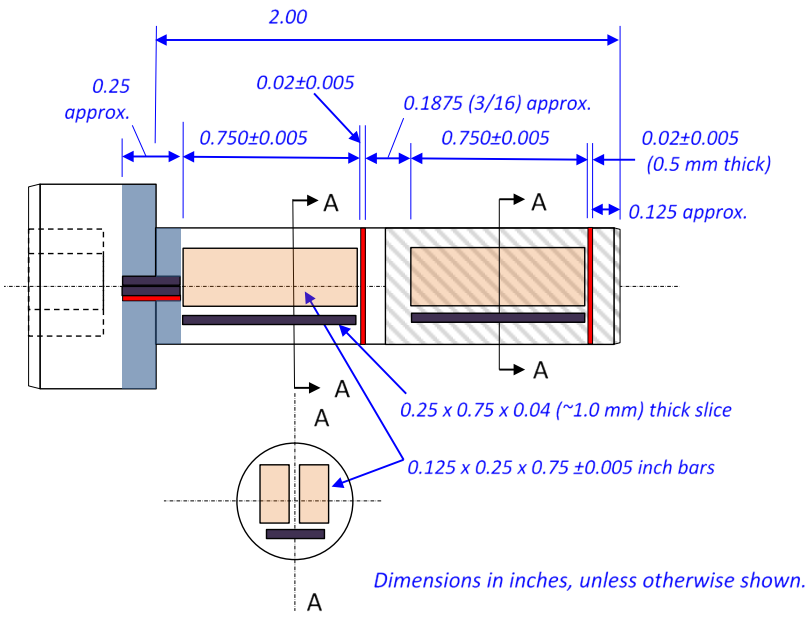

***Figure 2**: Machining diagram for the BFBs showing the color-coded sample types (red: 0.5 mm slices, black: 1.0 mm slices, light orange: bend bars, and light blue: remaining collar materials)* [12]

2.2 Characterization methods

Since it was revealed that the exposed surface of the bolts was still intact at the region where the bolt head meets the bolt shank, further characterization was performed on this region of the collar slice. The collar slice or CS section of both BFB #4412 and #4416 were characterized. The cross-section near the curved region was investigated for cracks that may hint at in-service IASCC. The cross-section of the near-surface area in the curved region was characterized by scanning electron microscopy (SEM)-electron backscatter diffraction (EBSD) using a Tescan Mira3 SEM equipped with an Oxford Instruments Symmetry S2 EBSD detector. Transmission electron microscopy (TEM) liftouts normal to the surface were made using a Thermo Fisher Versa3D focused ion-beam (FIB)/SEM. The TEM sample preparation followed the procedures of initial trenching, cutting, and thinning to 200 nm with 30 keV Ga^+ beam, thinning to ~100 nm with the ion beam energy gradually reduced to 2 keV. Before loading into the TEM, samples were cleaned with a Fischione 1020 Nanomill for 10 minutes on each side using 900 eV Ar^+. Microstructural characterization was performed with transmission Kikuchi diffraction (tKD) using the Tescan Mira3 SEM, and TEM/ scanning TEM (STEM) with energy-dispersive spectroscopy (EDS)-based mapping using a Thermo Fisher Talos F200X TEM/STEM equipped with a quadrupole SuperX Si-drift detector EDS system, a high resolution Gatan Ceta camera, and bright field (BF) and three annular dark field (ADF) detectors – low angle ADF (LAADF), medium angle ADF (MAADF), and high angle ADF (HAADF).

3. RESULTS AND DISCUSSION

3.1 Characterization of IASCC

Part of the collar slice or bolt head/shank intersection region was exposed to the primary water coolant in the two-loop downflow Westinghouse PWR [13]. The CS slice in these bolts still had the exposed surface retained without excessive handling or processing damage, as shown by the SEM image of the BFB #4412 surface in Figure 3. The SEM analysis of the surface showed the oxide layer with multiple fine cracks and rough particles which are Fe-rich oxide.

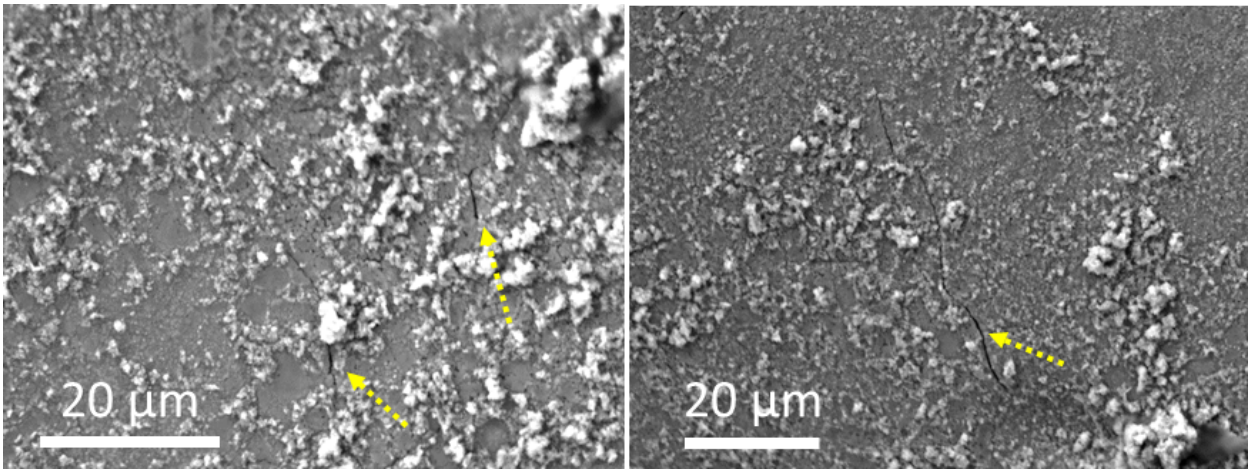

Figure 3*: Secondary electron SEM images of the surface of the head/shank transition area of BFB #4412. There are multiple small crack visible (yellow arrows) and rough Fe-rich oxide particles across surface.*

SEM analysis of the cross-section, as shown in BFB #4412 in Figure 4, demonstrated multiple small cracks along the specimen edge; all observed cracks were located inside the curved area, where stress would be highest. The longest crack reached ~6 µm. Based on the EBSD data, the corrosion crack readily propagated along random high-angle grain boundaries (RHAB) and actually splits into two different directions at a triple junction of RHABs. Special boundaries such as low-angle grain boundaries (LAGB) or twin boundaries (sigma-3 [Σ3]) appear to be immune from cracking as seen in Figure 4c, where the crack deflects and only travels along the RHAB despite hitting a triple junction of RHAB hitting a RHAB and a Σ3 boundary. Cracks propagated in the direction, normal to the surface suggesting the stress corrosion nature of this particular crack. In the near surface region, there is also evidence for localized deformation in the form of dislocation channels as highlighted in the EBSD maps. An oxidation environment, localized mechanical stress, and irradiation are present and make the material susceptible to IASCC. To investigate further the oxidation behavior and grain boundary attack at the cracks, targeted FIB liftouts were taken from the oxidized surface at cracks. One such liftout is shown in Figure 5 for BFB #4412. The STEM-ADF image and tKD maps in Figure 5 highlight the features that will be discussed further in full through this document: complex surface oxidation, grain boundary oxidative attack and cracking, and localized deformation in the form of dislocation channels.

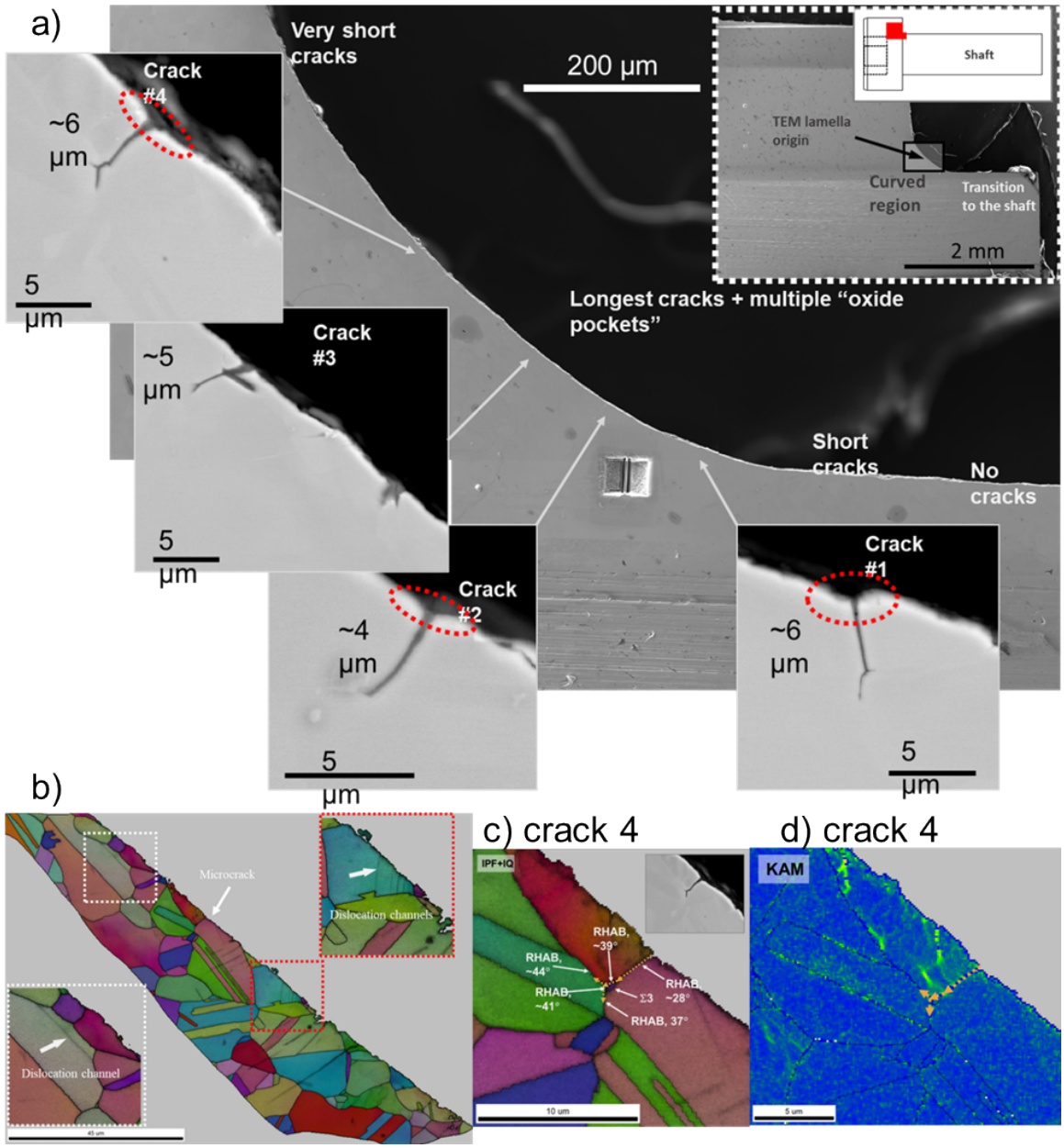

Figure 4*: SEM images from the curved section of BFB #4412 where the bolt head meets the bolt shank. Microscale cracks indicative of IASCC are found in the curved region and not in the straight regions.*

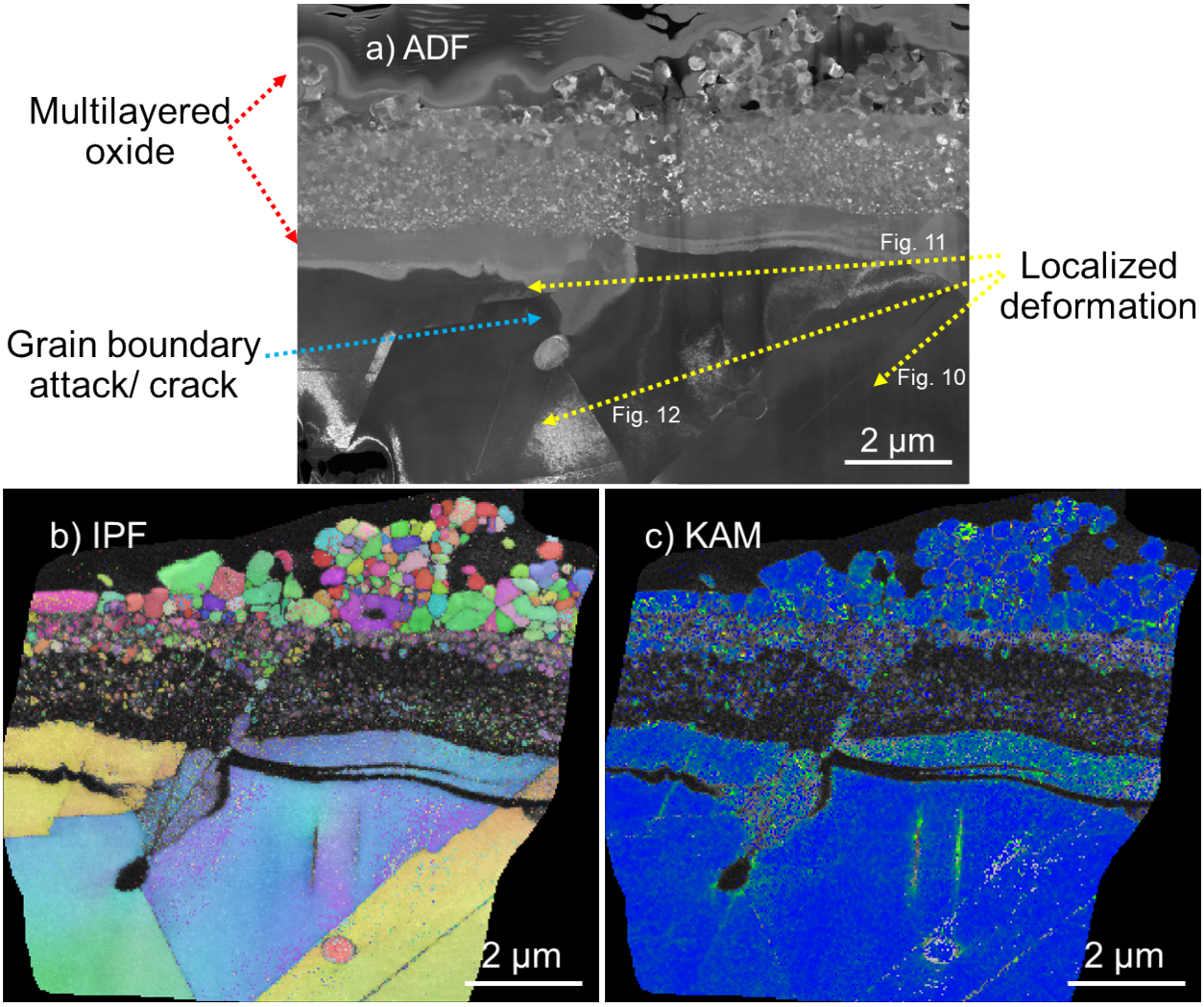

Figure 5: *a) STEM-ADF image of liftout from BFB #4412 taken from oxidized surface near "crack #4" in Figure 4. b) tKD IPF and c) KAM maps of the same liftout. Multiple features are apparent including a multilayered oxide (red arrows), grain boundary attack (blue arrow), and localized deformation features inside the bolt (yellow arrows). These localized deformation features will be discussed in Figures 10-12.*

3.2 Surface oxidation and grain boundary attack

The surface oxide on the curved section of the BFBs is complex. The STEM images, tKD IPF map, and EDS map for BFB #4412 in Figure 6 highlight the five distinct layers of the surface oxide that separate themselves by composition and by grain size. Interestingly, instead of five layers, only three layers are commonly identified for corrosion and radiation-enhanced corrosion [14,15]. This finding alone signals the need for extended radiation and corrosion studies, including studying the effect of dose rate. The total oxide thickness for this BFB is ~3 µm near its thinnest point and up to ~5 µm near grain boundaries. The outer most oxide layer, denoted as layer 1, is an Fe-rich oxide with large grains ~250-500 nm in size. The thickness of this layer varies from one grain thick (~250 nm) to multiple grains but seems to be largest around grain boundaries. The second layer is an intermixed Fe/Ni-rich and Cr-rich oxide with grain sizes of ~100-200 nm and a thickness of about 600-700 nm. The grains appear to be Fe/Ni-rich while the oxide boundaries are Cr-rich. The third layer is similar in composition to layer 2 but is marked by a much finer grain size of well under 100 nm. For this BFB #4412, this layer is ~1.3 µm thick. As is shown in Figure 8, this oxide layer thickness can vary substantially from bolt to bolt (only ~150-400 nm for the sample taken from BFB #4416). The fourth and fifth oxide layers appear monolithic in nature but are segregated by

composition with the fourth layer being Cr/Fe/Ni-rich while the fifth layer closest to the alloy surface is depleted in Fe and Ni. Layer 5 may also be amorphous as the tKD mapping was unable to index any Cr-rich crystalline oxide. The composition gradient of each layer, 1 through 5, are shown in 1-D composition profiles in Figure 7c/d. Each of layers 4 and 5 are ~300 nm, which is about the same thickness as in BFB #4416 in Figure 8. The total thickness of the surface oxide in BFB #4416 in Figure 8 and Figure 9 is ~1.7-2 µm, or about two-thirds the thickness of the oxide in BFB #4412. This could be due to multiple reasons, such as the following: (1) the thickness of the oxide likely can vary locally within the same bolt; (2) the radiation dose is different and could affect oxide formation; and (3) the PWR water conditions and flow could be slightly different.

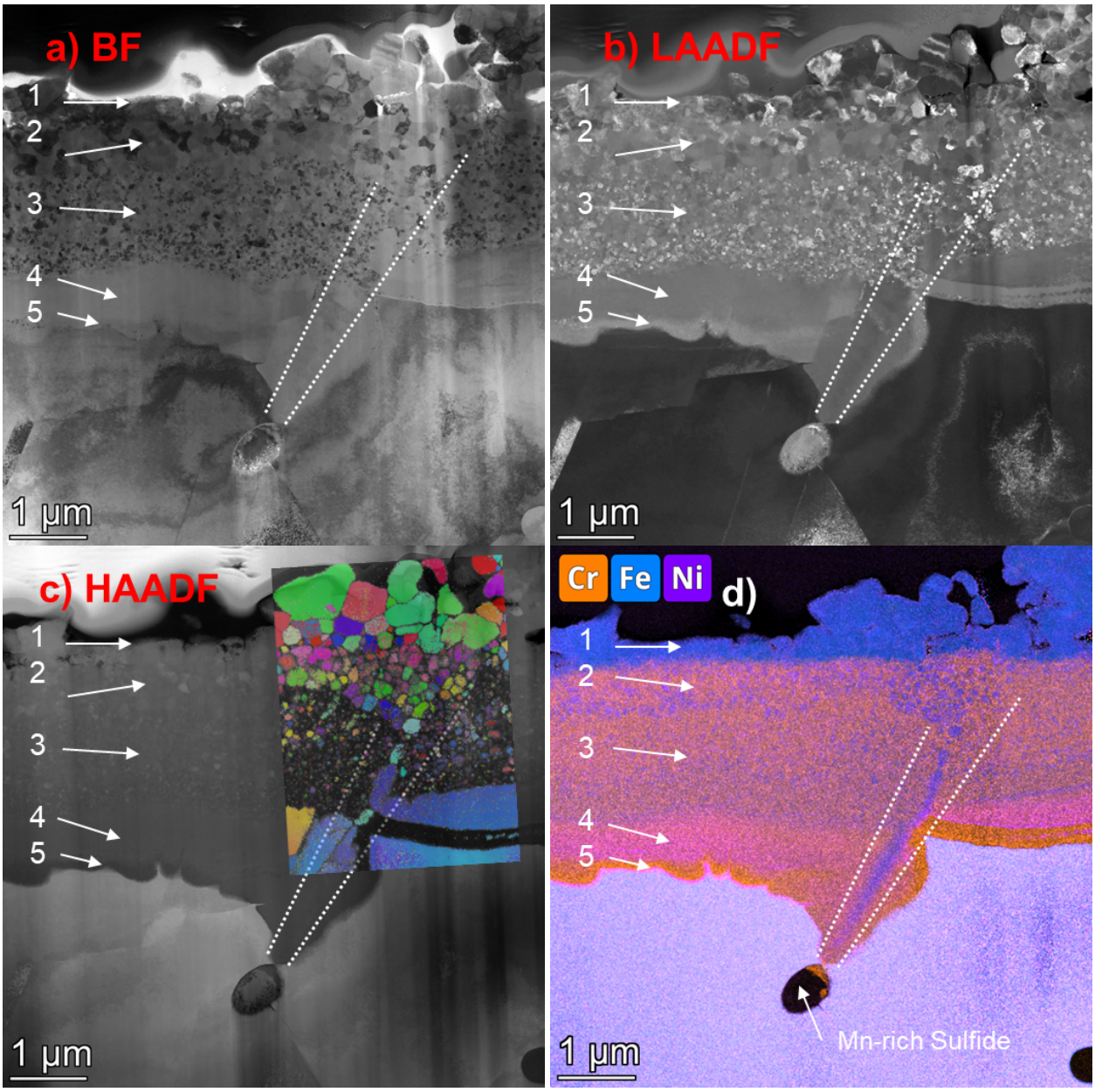

Figure 6: *a) STEM-BF, b) STEM-LAADF, c) STEM-HAADF with tKD-IPF map overlayed, and d) STEM-EDS Cr/Fe/Ni map of BFB #4412 highlighting the multilayered oxide and grain boundary attack. Numbers correspond with each oxide layer based on grain size and composition. The two near-parallel dotted lines highlight pathway along the grain boundary for Fe/Ni to out layers.*

Figure 6 and Figure 7 also highlight the interesting oxidative grain boundary attack. The near-parallel dotted lines in Figure 6 highlight two features: the grain boundary oxide is enriched in Fe or conversely depleted in Cr and the grain size is much larger than the oxides in layers 3, 4, and 5 away from the grain boundary. The grain boundary acts a diffusional pathway or pipeline for Fe and Ni to move to the outer oxides, especially layer 1 which is thickest around the grain boundary. The larger grains in layer 1 and 2 along the 'pipeline' are all enriched in Fe and Ni as highlighted in the concentration profiles in Figure 7e/f. This is likely exacerbated by radiation-induced segregation of Ni and Si to the grain boundary and depletion of Cr at the grain boundary. This same behavior observed in BFB #4412 can also be seen in BFB #4416 as layer 3 is clearly interrupted by larger grains near the grain boundary in Figure 8 and the original grain boundary location within the oxide is enriched in Fe and Ni and depleted in Cr as shown in Figure 9. Radiation-induced segregation not only enhances grain boundary attack, but it also enhances external oxide growth.

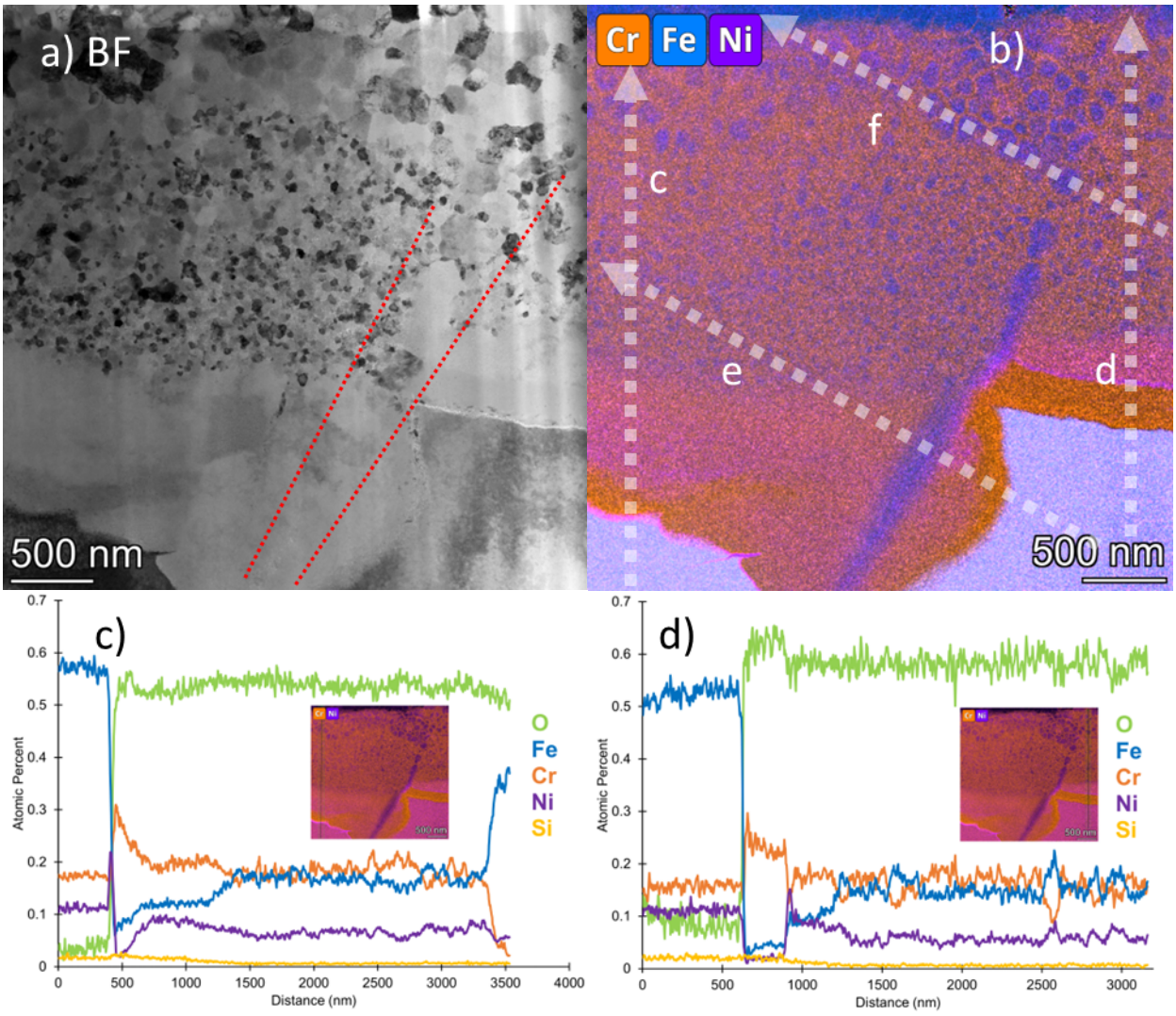

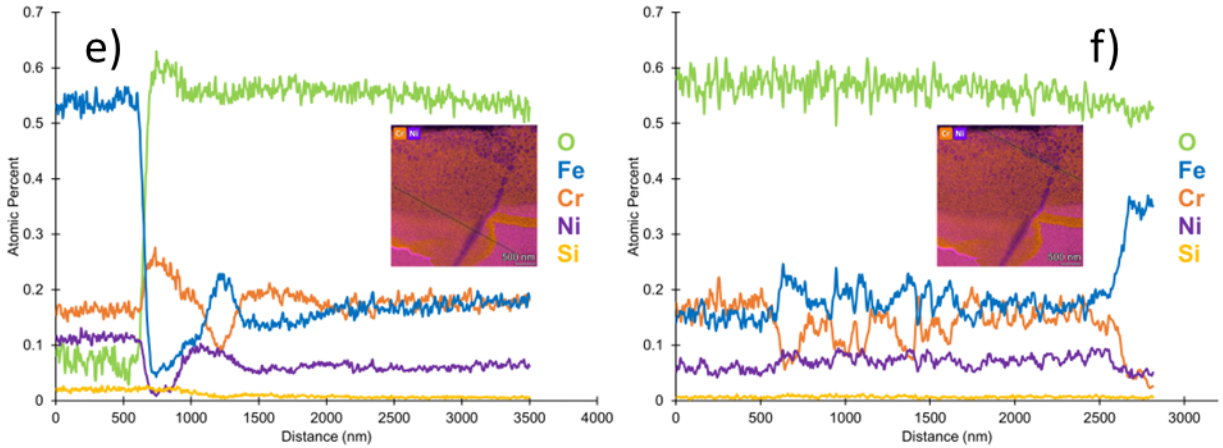

Figure 7: *Liftout from oxide of curved region in BFB #4412. a) STEM-BF image and STEM-EDS map of Cr/Fe/Ni overlayed showing oxide and grain boundary attack. (c-f) Concentration profiles corresponding to arrows in (b).*

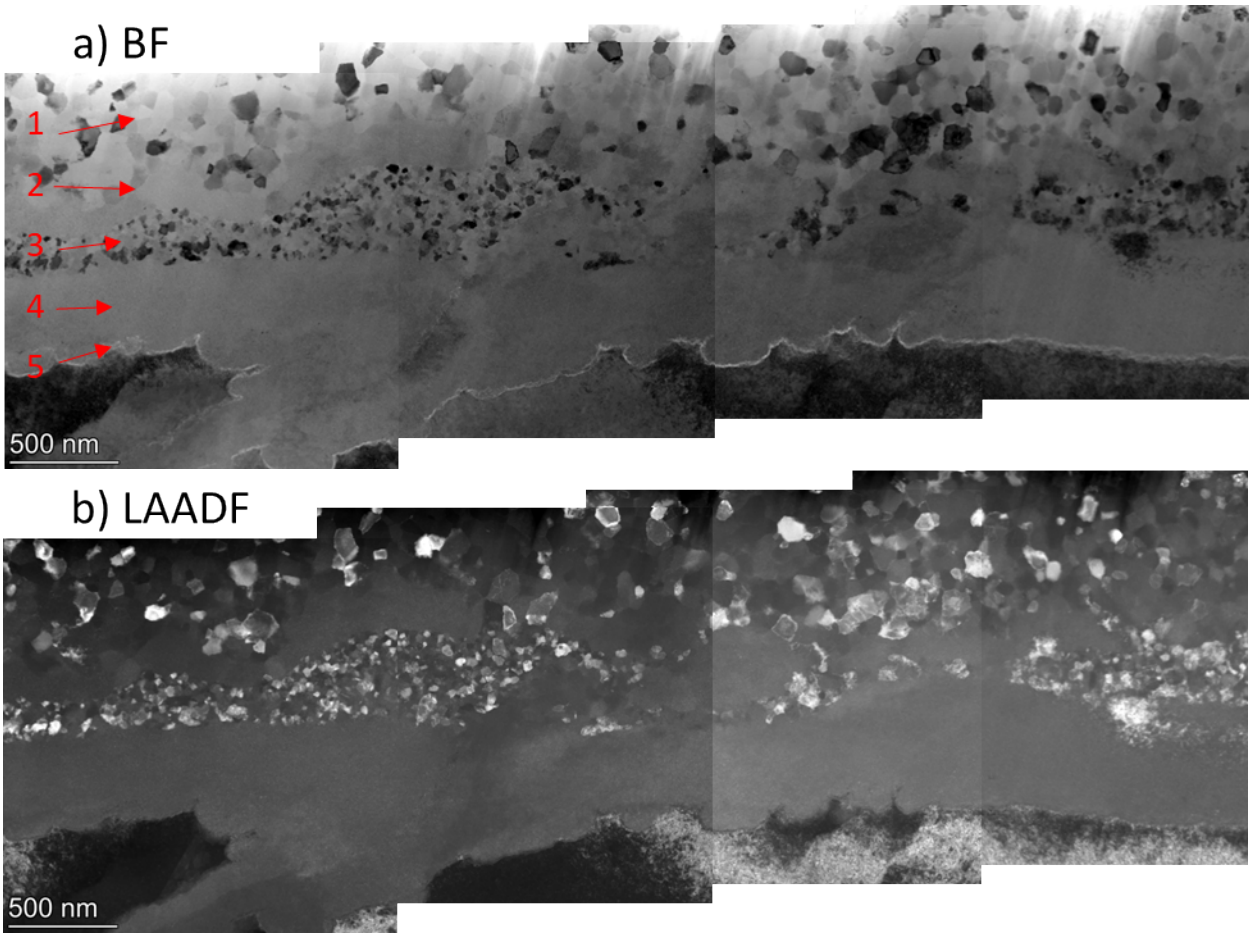

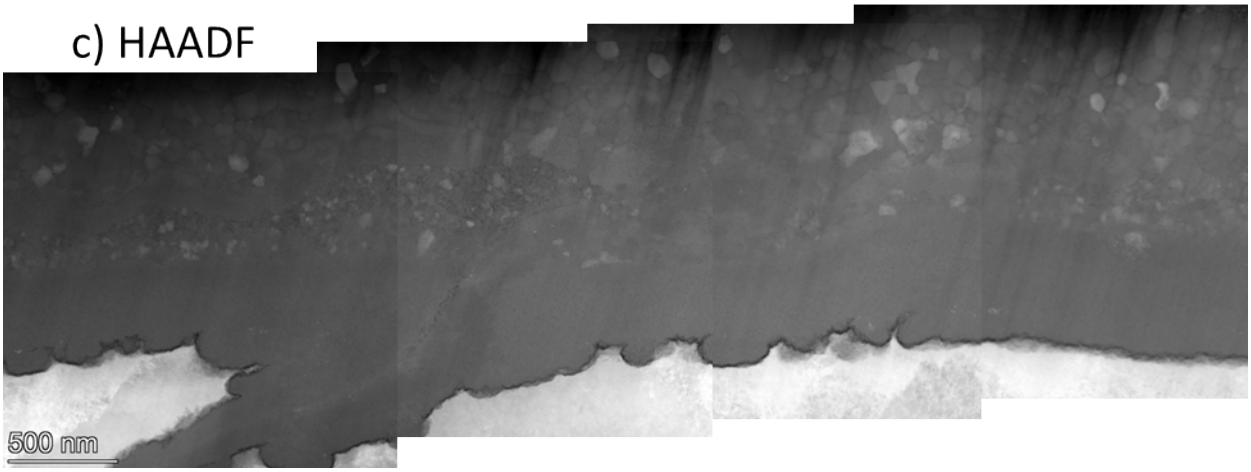

Figure 8: *a) STEM-BF, b) STEM-LAADF, c) STEM-HAADF images stitched together of surface oxide near an oxidized grain boundary in BFB #4416 highlighting the multilayered oxide and grain boundary attack. Numbers correspond with each oxide layer based on grain size and composition.*

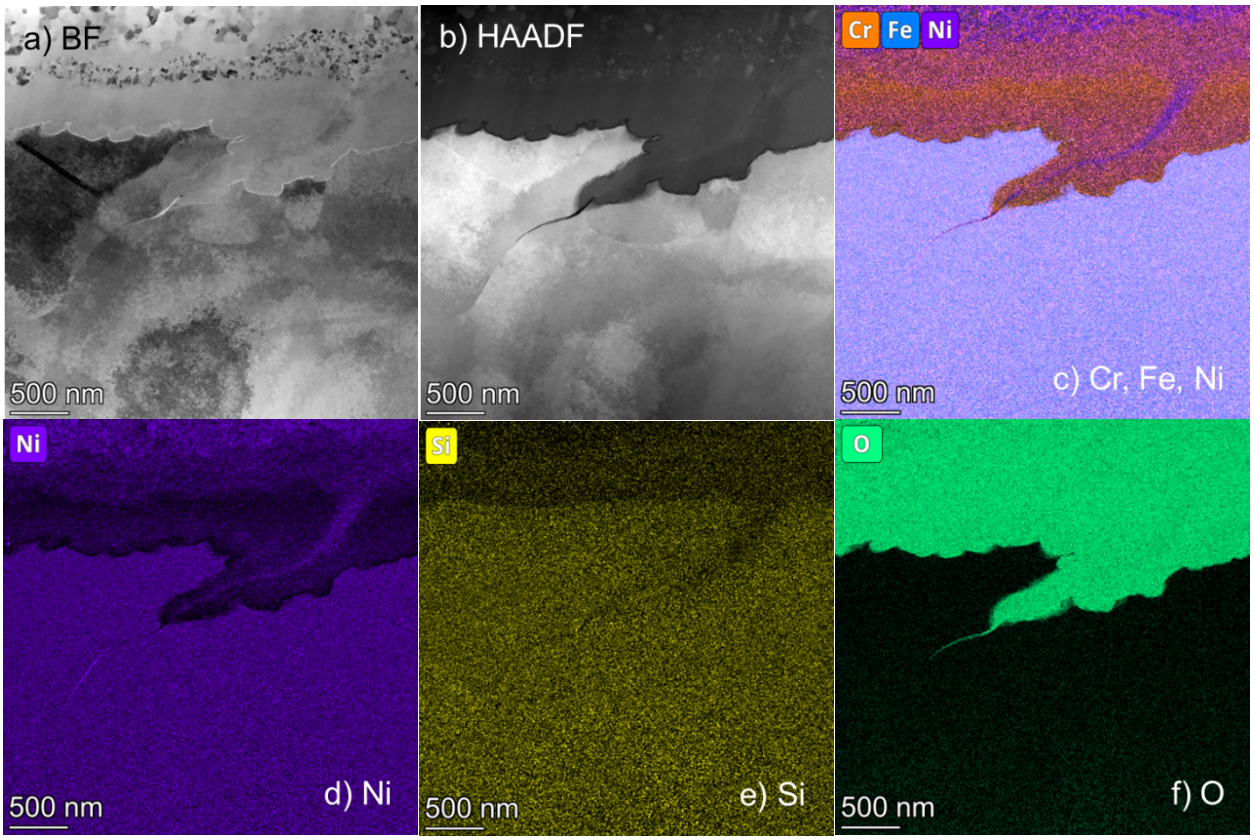

Figure 9: *Liftout from oxide of curved region in BFB #4416. a) STEM-BF and b) STEM-HAADF images showing oxide and grain boundary attack. STEM-EDS maps of c) Cr, Fe, Ni overlapped, d) Ni, e) Si, and f) O showing segregation of Ni at grain boundary but a depletion of Si near the oxidized grain boundary.*

3.3 Localized deformation and radiation induced segregation

Figure 10, Figure 11, and Figure 12 shows tKD and TEM/STEM analysis from different localized strain-induced features in the liftout in Figure 4.

The IPF map in Figure 10a shows the channel has a twin across its length based on the misorientation being about 60°, indicative of a strain-induced twin with two Σ3 boundaries. STEM-bright field (BF), STEM-EDS analysis, and TEM-BF imaging, as shown in Figure 10b-f, were conducted at the same ~50 nm wide feature. The most notable aspect is in the EDS map in Figure 10c showing clear segregation along channel boundaries. The surrounding matrix has a high density of Ni/Si-rich clusters, but there is an excess of clusters along the boundaries. The EDS concentration profile in Figure 10d shows the Ni/Si enrichment corresponds with a depletion of Cr, Mo, and Mn; there may be a slight enrichment of P within the channel though it is minimal. Additionally, the Ni and Si concentration between the boundaries is below that of the matrix outside the channel. The lack of precipitates between the boundaries suggests this is a defect-free dislocation channel, the result of localized deformation. There may also be a denuded zone where there is a slight reduction of Ni/Si relative to the matrix just outside the channel. Qualitatively, these results agree with previous studies on radiation-induced segregation (RIS) to Σ3 grain boundaries. [16–18].

The lack of precipitates inside the channel does not mean that no defects are observed within the channel. Nanoscale cavities and dislocation loops are observed within the channel in the under-focus TEM-BF images in Figure 10e and the TEM-BF image in Figure 10f, respectively. The nanocavities are in high density throughout the matrix just as reported elsewhere [8]. There appear to be fewer cavities within the channel, though it is difficult to quantify if there is a significant difference between the matrix and within the channel boundaries. However, there do appear to be cavities that build up on the channel boundaries as denoted by the dotted arrows. Similarly, the dislocation loop density appears to be much lower within the channel than in the matrix. Taken together, the total density of defects including precipitates, nanocavities, and dislocation loops are lower within the channel.

Although segregation at Σ3 boundaries, particularly coherent Σ3 boundaries, is weaker compared to random high-angle grain boundaries (RHAGBs) [17], this process cannot be dismissed. While there is evidence of twinning in the channel in Figure 10, destruction of Ni/Si-rich precipitates suggests the passage of multiple dislocations along the channel, since a single twinning event would likely be insufficient to destroy precipitates [19]. The motion of dislocations, especially through heavy or severe deformation, has been shown to dissolve precipitates [20,21] and is likely what happens here at the local scale.

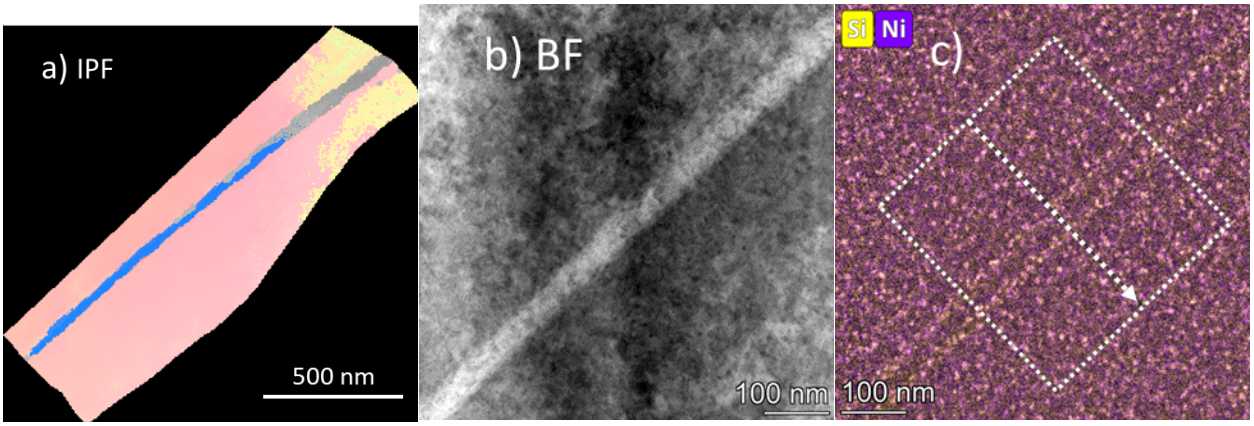

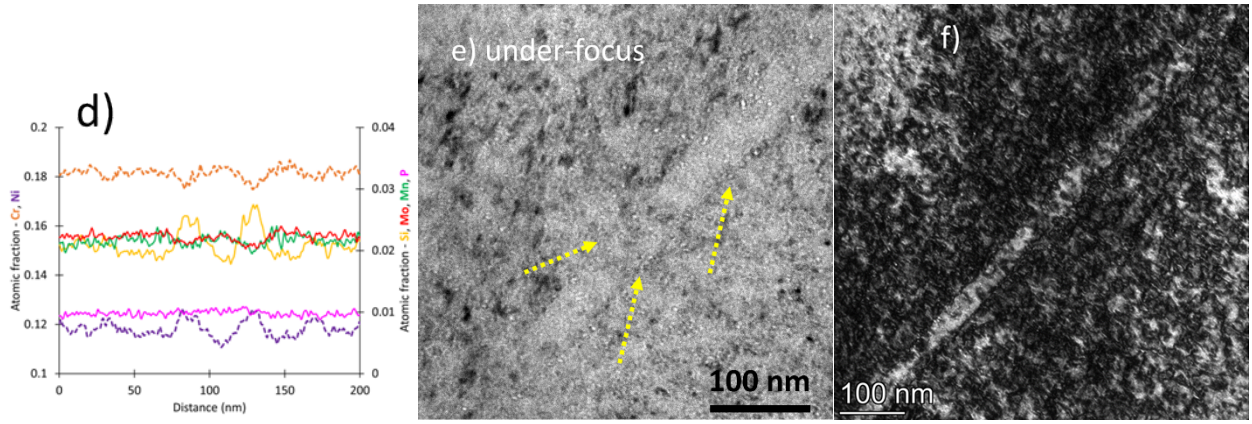

Figure 10: *a) tKD IPF map with 5 nm step size showing strain induced channel with deformation twin occupying most of the channel; b) STEM-BF and c) STEM-EDS Ni and Si map of same channel; d) concentration profile based on box in c) across the channel; e) under-focus TEM-BF images highlighting nanocavities including those along channel boundaries (arrows); and f) TEM two-beam BF image showing dislocation loops in matrix and channel.*

Similar STEM-EDS analyses were completed on other channel and localized defect features as well, as shown in Figure 11 and Figure 12, which are from the same liftout from BFB #4412. The region in Figure 11 shows two localized dislocation channels – the near vertical one (marked as d) and the horizontal one (marked as e). The near-vertical channel has extensive Ni/Si segregation and Cr/Mo/Mn depletion at the channel boundaries, more so than the channel boundaries in Figure 10. Two maximums in Si and Ni curves in the near-vertical channel in Figure 11d suggest strain-induced twins occupying a portion of the channel. However, instead of discrete precipitates, the segregation to the channel boundaries appears to be smooth here and reaches a much higher level than the channel in Figure 10. The BF and LAADF images show there is some but relatively low dislocation content within the channel. The horizontal channel on the other hand has elongated diffraction features as dislocations passed along it. This channel intersects with the other channel and looks like it causes channel 'd' to bend or be compressed slightly (the bending is pointed by dashed arrow in Figure 11). This horizontal channel does have some slight Ni/Si segregation to it as shown in the concentration profile in Figure 11 but no evidence of a strain-induced twin. The higher degree of segregation at the near-vertical channel 'd' boundaries also means these boundaries may likely be incoherent Σ3 boundaries due to being a good sink for defects and solute and comparable to RHAGBs [17]. The segregation to the non-twinned channel suggests that localized strain-induced features can serve as sinks for defects and solutes just as a dislocations and dislocation cells can [22].

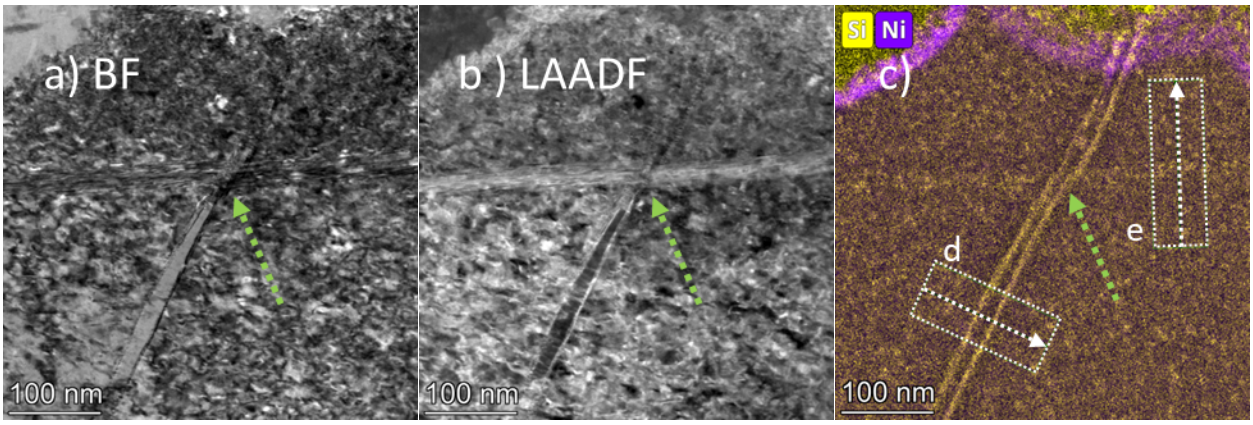

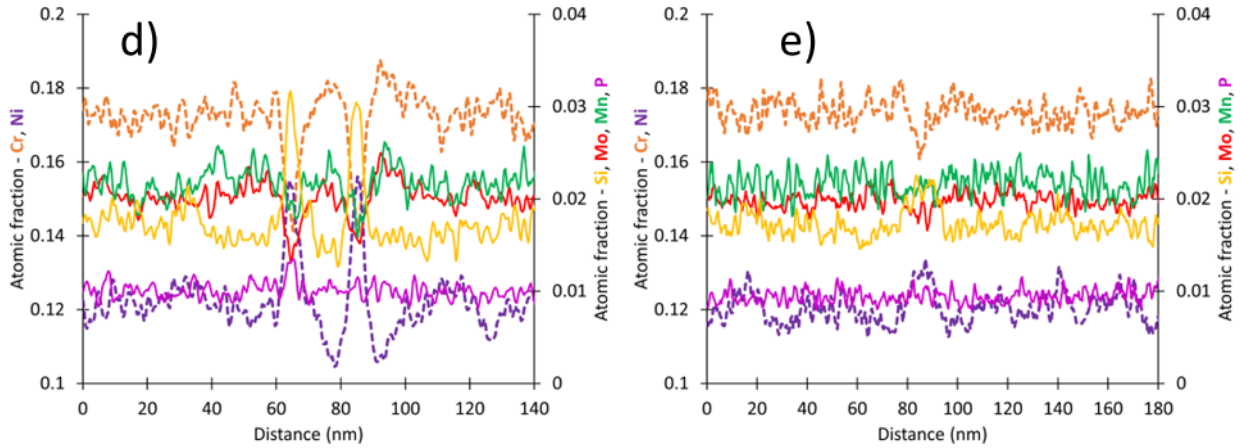

Figure 11: *a) STEM-BF, b) STEM-LAADF, and c) STEM-EDS Ni and Si map showing dislocation channel (d) with likely internal twin intersecting with another dislocation channel (e); d) concentration profile based on box in c) across the channel with twin; e) concentration profile based on box in c) across the untwinned channel*

The third localized deformation feature near the sulfide inclusion from Figure 5 is characterized with tKD, STEM imaging, and STEM-EDS mapping in Figure 12. In the STEM in Figure 12a/b, one may see two grains, G_1 and G_2, as well as a dislocation channel (Ch) that nearly intersects with a grain boundary at a sulfide inclusion (S_{inc}). The grain boundary between G_1 and G_2 is a RHAGB. The EDS map, Figure 12c, show obvious segregation inside the channel. STEM-EDS performed at elevated magnification, Figure 12d/e, does not show evidence of twinnig. One may see also much larger Ni/Si-rich precipitates but no general segregation, Figure 12f. The band contrast and IPF maps, Figure 12g/h, show minimal change across the channel, but the KAM map, Figure 12i, highlights there is increased KAM values at the channel that is similar to the grain boundary between G_1 and G_2. The STEM imaging and EDS analysis in Figure 12e-f, shows the channel is similar to the horizontal channel in Figure 11 with elongated features, but it does not have any twin character. In this sense, there are not clear channel boundary walls like the twinned-channels in Figure 10 and Figure 11. This suggests that localized strain-induced features can serve as sinks for defects and solutes just as a dislocations and dislocation cells can [22].

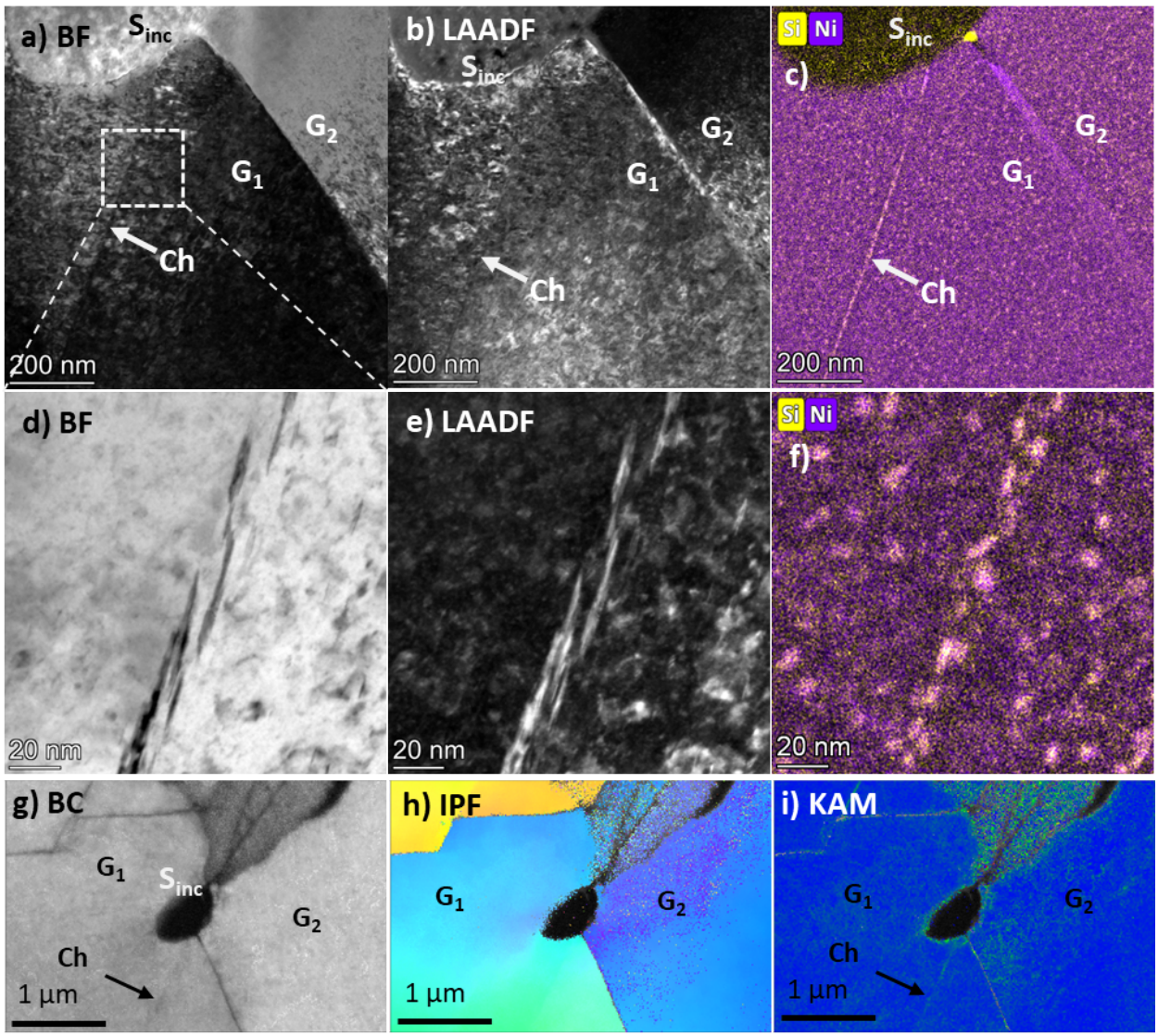

Figure 12: *a) STEM-BF, b) STEM-LAADF image, and c) STEM-EDS Ni and Si map of channel and grain boundary showing channel nearly intersecting with a random high angle grain boundary at a sulfide inclusion; d) STEM-BF, e) STEM-LAADF image, and f) STEM-EDS Ni and Si map zoomed in on the zoomed in on the channel, but tilted to a kinematical condition. g, h, i) tKD band contrast, IPF, and KAM maps, respectively.*

This secondary radiation-induced segregation and precipitation at channels and channel boundaries strongly suggests that the defect-free channel contribution to different phenomena (e.g., dislocation channeling as a driving force for IASCC [6]) may extend beyond purely mechanical effect and contribution of dislocation pileups [23], observed in model experiments with pre-irradiated materials. Dislocation channels may serve as traps for defects as evidenced by the precipitates that formed along them. However, they could also serve to enhance solute diffusion [24,25] as the degree of strain locally can reach greater than 100% [26]. A synergistic effect could also take place as dislocations create a higher concentration of solute locally [19], which could mediate solute diffusion towards the grain boundary while also creating solute trapping sites with the matrix enabling precipitation along the channel walls. This change in solute concentration locally may affect not only the mechanical stress and strain locally but also the response to corrosive environments. Enhanced Ni/Si segregation in the in-service formed channels may lead to variations in local corrosion behavior on a sub-grain scale, which could further enhance susceptibility to IASCC. The observed behavior

here in harvested materials needs additional, focused investigation through controlled experiments with the exact stress level and loading event timing. As such, this highlights the importance for characterization of harvested materials. Not only can laboratory-based or test-reactor-based research findings be validated, but also new insights can be brought to the forefront since the ‘real world’ conditions are relatively unique compared to laboratory conditions.

4. CONCLUSIONS

In this report, we present our latest study in FY24 on microstructural characterization on the IASCC features within both high fluence PWR BFBs: general oxidation, grain boundary attack, and localized deformation via dislocation channeling. The objective of this work is to provide information that is integral to evaluating end of life microstructure and properties for developing models for predicting radiation-induced swelling, segregation, precipitation, mechanical property degradation, and now IASCC susceptibility. The main findings are summarized as follows:

1. Complex multilayered surface oxide formation: The surface oxide is ~2-3 μm thick depending on the bolt with five – not three – distinct layers that vary based on composition and grain size. The innermost layer is Cr-rich and Fe/Ni depleted. The next layer is both Cr and Fe/Ni-rich and is too monolithic in nature. In previous studies, these two layers are likely seen as one layer but are clearly found to be distinct here. The next two layers are also likely commonly seen as the same layer, but these Cr-rich and Fe/Ni-rich oxide layers are clearly distinguished primarily by grain size, with layer 3 being nanocrystalline and layer 4 being above ~100 nm in size. Layer 3 also was shown to vary most in its thickness between the two BFBs. Lastly, the outermost oxide is a Fe-rich oxide with large grain size of ~500 nm.
2. Grain boundary attack and pathway to outer oxide: The oxidized grain boundary attack features a pathway from the original grain boundary that is enriched in Fe/Ni and depleted in Cr that acts as a pathway for Fe/Ni to the outermost oxide layers. The grains along this path interrupt the nanocrystalline interior oxide layers as they are larger and depleted in Cr.
3. Localized deformation and elemental segregation: Localized deformation in the form of dislocation channels and deformation twins were observed. Along these channels, particularly the twinned channels, enhanced segregation and precipitation of Ni/Si was observed on the channel walls. The channels likely formed through heavy localized deformation clearing out defects. The channel eventually became less active, but radiation continued enabling diffusion, precipitation, and defect formation to resume in the vicinity of the channels. This could have implications for influencing segregation to grain boundaries and impacting susceptibility to IASCC.

5. REFERENCES

[1] Stress Corrosion Cracking in Light Water Reactors: Good Practices and Lessons Learned, INTERNATIONAL ATOMIC ENERGY AGENCY, Vienna, 2011. https://www.iaea.org/publications/8671/stress-corrosion-cracking-in-light-water-reactors-good-practices-and-lessons-learned.

[2] X. (Frank) Chen, T. Chen, C.M. Parish, T. Graening, M.A. Sokolov, K.J. Leonard, Post-Irradiation Examination of High Fluence Baffle-Former Bolts Retrieved from a Westinghouse Two-Loop Downflow Type PWR, ORNL/TM-2019/1251, United States, 2019. https://doi.org/10.2172/1557483.

[3] T.G. Lach, X. (Frank) Chen, T.M. Rosseel, Microstructural characterization of the second high fluence baffle-former bolt retrieved from a Westinghouse two-loop downflow type PWR, ORNL/TM-2022/2668, 2022. https://doi.org/10.2172/1897832.

[4] T.G. Lach, M.N. Gussev, X. (Frank) Chen, Microstructural Characterizations of Two High Fluence Baffle-Former Bolts Retrieved from a Westinghouse Two-Loop Downflow Type PWR, 2023.

[5] X. (Frank) Chen, M.A. Sokolov, Fracture Toughness and Fatigue Crack Growth Rate Testing of Baffle-Former Bolts Harvested from a Westinghouse Two-Loop Downflow Type PWR, ORNL/TM-2021/2264, 2021.

[6] G.S. Was, C.-B. Bahn, J. Busby, B. Cui, D. Farkas, M. Gussev, M. Rigen He, J. Hesterberg, Z. Jiao, D. Johnson, W. Kuang, M. McMurtrey, I. Robertson, A. Sinjlawi, M. Song, K. Stephenson, K. Sun, S. Swaminathan, M. Wang, E. West, How irradiation promotes intergranular stress corrosion crack initiation, Prog. Mater. Sci. 143 (2024) 101255. https://doi.org/10.1016/j.pmatsci.2024.101255.

[7] X. (Frank) Chen, K.J. Leonard, M.A. Sokolov, M.A. Burke, M.N. Gussev, S.R. Clark, Specimen Fabrication from Two High Fluence Ginna Baffle Bolts, ORNL/TM-2017/455, 2017.

[8] T.G. Lach, X. (Frank) Chen, Post Irradiation Examination of Pressurized Water Reactor Stainless Steel Internal Components, in: Press. Vessel. Pip., 2023: p. 107347. https://doi.org/10.1115/PVP2023-107347.

[9] O.K. Chopra, A.S. Rao, Degradation of LWR Core Internal Materials due to Neutron Irradiation, NUREG/CR-7027, 2010.

[10] H.T. Tang, Materials Reliability Program Determination of Operating Parameters of Extracted Bolts (MRP-52), report number 1003076, EPRI technical report, 2001.

[11] D.J. Edwards, E.P. Simonen, F.A. Garner, L.R. Greenwood, B.M. Oliver, S.M. Bruemmer, Influence of irradiation temperature and dose gradients on the microstructural evolution in neutron-irradiated 316SS, J. Nucl. Mater. 317 (2003) 32–45. https://doi.org/10.1016/S0022-3115(03)00003-5.

[12] K.J. Leonard, M.A. Sokolov, M.N. Gussev, Post-Service Examination of PWR Baffle Bolts, Part I. Examination and Test Plan, Oak Ridge National Laboratory Report, ORNL/LTR-2015/193, 2015.

[13] M.R. Ickes, J. McKinley, J.-K. Lee, J.M. Smith, A.M. Ruminski, M.A. Burke, Irradiation-assisted stress corrosion cracking of Type 347 and Type 316 steels irradiated in commercial pressurized water reactors, J. Nucl. Mater. 536 (2020) 152182. https://doi.org/10.1016/j.jnucmat.2020.152182.

[14] H. Liu, G.-H. Lei, H.-F. Huang, Review on synergistic damage effect of irradiation and corrosion on reactor structural alloys, Nucl. Sci. Tech. 35 (2024) 57. https://doi.org/10.1007/s41365-024-01415-3.

[15] S. Wang, Q. Wang, S. Zhang, J. Xie, M. Song, W. Kuang, Clarifying the irradiation effect on the general oxidation of 316L stainless steel in high temperature hydrogenated water after 1000h immersion, Acta Mater. 255 (2023) 119100. https://doi.org/https://doi.org/10.1016/j.actamat.2023.119100.

[16] N. Sakaguchi, S. Watanabe, H. Takahashi, R.G. Faulkner, A multi-scale approach to radiation-

induced segregation at various grain boundaries, J. Nucl. Mater. 329–333 (2004) 1166–1169. https://doi.org/10.1016/j.jnucmat.2004.04.268.
[17] C.M. Barr, G.A. Vetterick, K.A. Unocic, K. Hattar, X.-M. Bai, M.L. Taheri, Anisotropic radiation-induced segregation in 316L austenitic stainless steel with grain boundary character, Acta Mater. 67 (2014) 145–155. https://doi.org/10.1016/j.actamat.2013.11.060.
[18] S. Watanabe, Y. Takamatsu, N. Sakaguchi, H. Takahashi, Sink effect of grain boundary on radiation-induced segregation in austenitic stainless steel, J. Nucl. Mater. 283–287 (2000) 152–156. https://doi.org/10.1016/S0022-3115(00)00204-X.
[19] Z. Jiao, M.D. McMurtrey, G.S. Was, Strain-induced precipitate dissolution in an irradiated austenitic alloy, Scr. Mater. 65 (2011) 159–162. https://doi.org/10.1016/j.scriptamat.2011.04.003.
[20] Y. Ashkenazy, N.Q. Vo, D. Schwen, R.S. Averback, P. Bellon, Shear induced chemical mixing in heterogeneous systems, Acta Mater. 60 (2012) 984–993. https://doi.org/10.1016/j.actamat.2011.11.014.
[21] S.N. Arshad, T.G. Lach, M. Pouryazdan, H. Hahn, P. Bellon, S.J. Dillon, R.S. Averback, Dependence of shear-induced mixing on length scale, Scr. Mater. 68 (2013). https://doi.org/10.1016/j.scriptamat.2012.10.027.
[22] J. Yang, L. Hawkins, Z. Shang, E.A. McDermott, B.K. Tsai, L. He, Y. Lu, M. Song, H. Wang, X. Lou, Dislocation channel broadening–A new mechanism to improve irradiation-assisted stress corrosion cracking resistance of additively manufactured 316 L stainless steel, Acta Mater. 266 (2024) 119650. https://doi.org/10.1016/j.actamat.2024.119650.
[23] G.S. Was, D. Farkas, I.M. Robertson, Micromechanics of dislocation channeling in intergranular stress corrosion crack nucleation, Curr. Opin. Solid State Mater. Sci. 16 (2012) 134–142. https://doi.org/10.1016/j.cossms.2012.03.003.
[24] S. Odunuga, Y. Li, P. Krasnochtchekov, P. Bellon, R.S. Averback, Forced Chemical Mixing in Alloys Driven by Plastic Deformation, Phys. Rev. Lett. 95 (2005) 45901. https://doi.org/10.1103/PhysRevLett.95.045901.
[25] M. Wang, R.S. Averback, P. Bellon, S. Dillon, Chemical mixing and self-organization of Nb precipitates in Cu during severe plastic deformation, Acta Mater. 62 (2014) 276–285. https://doi.org/10.1016/j.actamat.2013.10.009.
[26] M.D. McMurtrey, G.S. Was, B. Cui, I. Robertson, L. Smith, D. Farkas, Strain localization at dislocation channel–grain boundary intersections in irradiated stainless steel, Int. J. Plast. 56 (2014) 219–231. https://doi.org/10.1016/j.ijplas.2014.01.001.